Metallic Carbon Nanotube Nanocavities as Ultra-compact and Low-loss Fabry-Perot Plasmonic Resonators

Sheng Wang[1,2], *Fanqi Wu*[3], *Kenji Watanabe*[4], *Takashi Taniguchi*[4], *Chongwu Zhou*[3,5], *Feng Wang**[1,2,6]

[1]Department of Physics, University of California at Berkeley, Berkeley, California 94720, USA.

[2]Materials Science Division, Lawrence Berkeley National Laboratory, Berkeley, California 94720, USA.

[3]Department of Chemical Engineering and Materials Science, University of Southern California, Los Angeles, California 90089, United States

[4]National Institute for Materials Science, 1-1 Namiki, Tsukuba 305-0044, Japan.

[5]Department of Electrical Engineering, University of Southern California, Los Angeles, California 90089, United States

[6]Kavli Energy NanoSciences Institute at the University of California, Berkeley and the Lawrence Berkeley National Laboratory, Berkeley, California, 94720, USA.

*Correspondence to: fengwang76@berkeley.edu

Abstract: Plasmonic resonators enable deep subwavelength manipulation of light matter interactions and have been intensively studied both in fundamental physics as well as for potential technological applications. While various metallic nanostructures have been proposed as plasmonic resonators, their performances are rather limited at mid- and far-infrared wavelengths. Recently, highly-confined and low-loss Luttinger liquid plasmons in metallic single walled carbon nanotubes (SWNTs) have been observed at infrared wavelengths. Here, we tailor metallic SWNTs into ultraclean nanocavities by advanced scanning probe lithography and investigate plasmon modes in these individual nanocavities by infrared nano-imaging. The dependence of mode evolutions on cavity length and excitation wavelength can be captured by a Fabry-Perot resonator model of a plasmon nanowaveguide terminated by highly reflective ends. Plasmonic resonators based on SWNT nanocavities approach the ultimate plasmon confinement limit and open the door to the strong light-matter coupling regime, which may enable various nanophotonic applications.

KEYWORDS: Plasmonic nanocavity, Carbon nanotubes, Infrared nano-imaging, Nanophotonics

Introduction

Surface plasmons, collective electromagnetic excitations coupled to conduction electron oscillations, enable the confinement of light to scales far beyond the diffraction limit of conventional optics. Plasmonic resonators take advantage of these unique capabilities and show tantalizing potentials in manipulation of light matter interaction at the nanoscale[1-4]. Currently, plasmonic resonators based on noble metallic nanostructures typically operate in the visible and near-infrared range but are hindered by a trade-off between optical field confinement and losses imposed by Landau damping[5,6]. Alternatives such as phonon polaritons in polar crystals are constrained to the Reststrahlen bands and cannot achieve broadband response[7,8]. Luttinger liquid plasmons in metallic single walled carbon nanotubes (SWNTs) are free from Landau damping[9]. Recently, these quantum plasmons in metallic SWNTs at infrared frequencies have been observed and demonstrated to exhibit the combination of low dispersion, deep subwavelength confinement (mode volume $<10^{-8}\ \lambda_0^{\,3}$) and high quality factor ($Q > 10$)[10,11]. Here, we show that tailored metallic SWNT nanocavities act as ultra-compact and low-loss Fabry-Perot plasmonic resonators with exceptional tunability. We trim long metallic SWNTs into ultraclean nanocavities of different sizes by advanced scanning probe lithography (SPL)[12-14].

Plasmon modes in these different nanocavities are then probed with spectrally resolved infrared nano-imaging. We find that plasmon modes in nanotube nanocavities depend sensitively on cavity length and excitation wavelength. Detailed mode evolutions are visualized when the plasmon wavelength is tuned to be on and off resonance with the cavity modes. These high-quality plasmonic resonators promise as a useful ultracompact plasmonic component in nanophotonic circuitry and also may enable strong light-matter interaction regime for study of quantum nano-optics, nonlinear nano-optics and ultracompact sensing[15-21].

Results and Discussion

High-quality SWNTs are directly grown by chemical vapor deposition (CVD) onto hexagonal boron nitride (h-BN) flakes exfoliated on SiO_2 (285 nm)/Si substrate (see Methods for details). Plasmons in these nanotubes are probed with an infrared scanning near-field optical microscope (IR-SNOM)[10,11]. This infrared nano-imaging technique is based on a tapping mode atomic force microscope (AFM) as schematically illustrated in Figure 1a (see Methods for details). In brief, a gold-coated AFM tip is illuminated with a quantum cascade laser (QCL) with tunable wavelength from 11.1 to 9.5 μm. The sharp AFM tip simultaneously excites plasmons in SWNTs and scatters the plasmon waves into the far field. The backscattered signal from the tip-sample system is captured by a mercury cadmium telluride (MCT) detector and carries essential near-field plasmon information about the sample. By scanning the tip along the nanotubes, plasmon modes can be visualized in real space. The near-field images are supplemented with in-situ AFM topography measurements, which provide the diameter and length of the nanotubes. Metallic nanotubes featuring Luttinger liquid plasmon oscillations are first identified and located using infrared nano-imaging. Nanotube M labeled in Figure 1c is a representative metallic nanotube and exhibits prominent oscillations in the near-field response at an excitation wavelength of 10.6 μm as shown in Figure 1d. These oscillation peaks arise from the constructive interference between the plasmon wave launched by the tip and the wave reflected by the nanotube end. The plasmon wavelength λ_p is thus twice the oscillation period. As the plasmon wave propagates, it is damped, as characterized by the quality factor Q. The near-field response along the nanotube is fitted to a damped oscillator form $e^{-2\pi x/(Q\cdot\lambda_P)}\sin\left((4\pi x)/\lambda_p\right)$, with x measured from the nanotube end. We then extract both the plasmon wavelength λ_P and the quality factor Q[10,11]. In contrast, nanotube S labeled in Figure 1c is a semiconducting

nanotube, which exhibits negligible infrared response due to the absence of free electrons (Figure 1d).

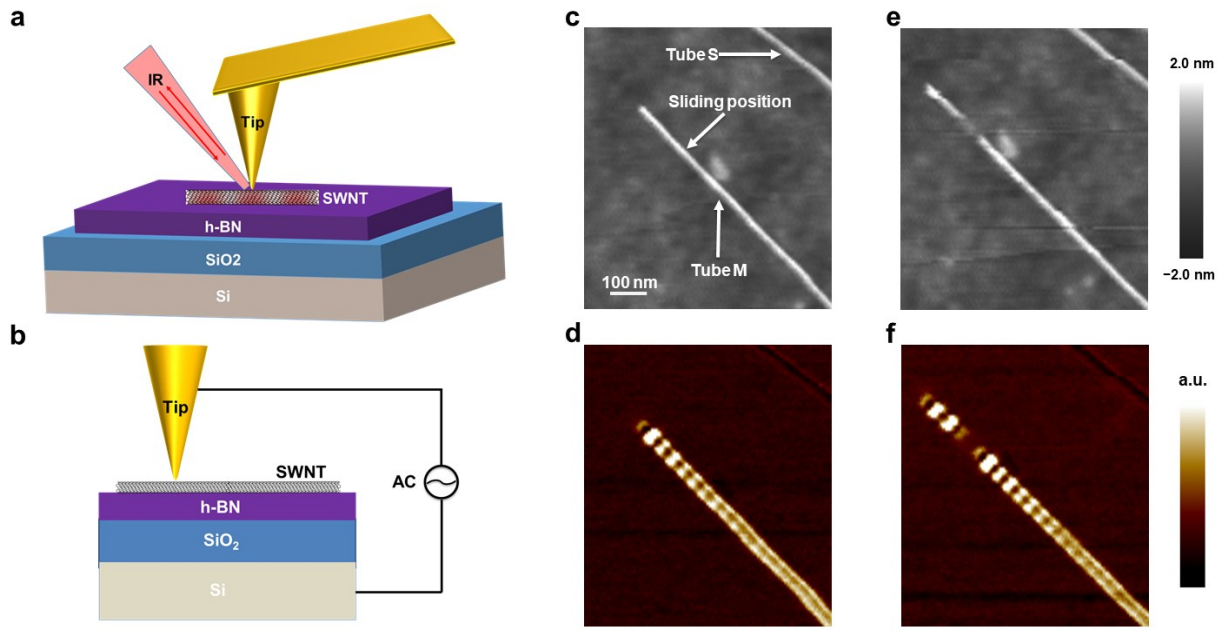

Figure 1. Infrared nano-imaging and scanning probe lithography of SWNTs. (a) Schematic of infrared nano-imaging of SWNTs. In brief, a gold-coated AFM tip is illuminated with a quantum cascade laser (QCL) with tunable wavelength from 11.1 to 9.5 μm. The backscattered signal from the tip-sample system carries essential plasmon information of the sample. By scanning the tip along the nanotubes, plasmon modes in the nanotubes can be visualized in real space. **(b)** Schematic of advanced scanning probe lithography. A high-frequency AC voltage is applied between the tip and the conductive Si layer of the substrate. Nanotube can be etched away due to oxidation of carbon by the oxygen-containing radicals generated between the tip and the nanotube. **(c)** Topography image of representative SWNTs. Tube M is a metallic SWNT whereas tube S is a semiconducting one. The white arrow labeled as sliding position indicates the nanoeteching position. **(d)** Corresponding near-field image to **(c)**. Metallic nanotube M exhibits prominent plasmon oscillations whereas semiconducting nanotube S shows little near-field response. **(e)** Topography of SWNTs after nanolithography. The nanolithography results in a SWNT nanocavity with length ~ 100 nm. **(f)** Corresponding near-field image to **(e)**. Plasmon modes in the nanocavity and the remaining long nanotube are visualized in real space. The

excitation wavelength is 10.6 μm for the infrared nano-imaging. **(c)** to **(f)** share the same scale bar as shown in **(c)**.

AFM-based SPL is used to trim the long metallic nanotubes into nanocavities. The process is schematically shown in Figure 1b. While the tip is engaged at the desired location and brought across the nanotube, a high-frequency (~ 40 kHz) alternating voltage is applied between the AFM tip and the conductive Si layer of the substrate[13] (see Methods for details). This voltage generates a high-frequency AC current which penetrates the SiO_2 layer via capacitive coupling effect. As a result, a localized strong electric field can form between the tip and the nanotube, which attracts polar H_2O molecules from air and also decomposes them into oxygen-containing radicals (e.g., OH^- and O^{2-}). Nanotubes can then be etched away due to oxidation of carbon by these oxygen-containing radicals. Notably, this SPL technique does not require prefabricated contact microelectrodes which are needed in conventional SPL to conduct DC current between the tip and the sample[12-14]. As a result, the nanotube nanocavities can remain ultraclean whereas conventional nanolithography techniques such as those based on electron or focused ion beams (Figure S1) can easily introduce defects or contaminants, compromising the quality of the nanocavities. Figure 1e shows a nanotube nanocavity cut at the position indicated by the white arrow in Figure 1c. The resulting cavity length is ~ 100 nm. Its plasmon mode, featuring two prominent symmetric peaks, is revealed by infrared nano-imaging (Figure 1f). The remaining larger nanotube with a newly defined end (Figure 1f) has a nearly identical infrared near-field response to the original uncut nanotube (Figure 1d), which points the cleanness of the nanoetching method.

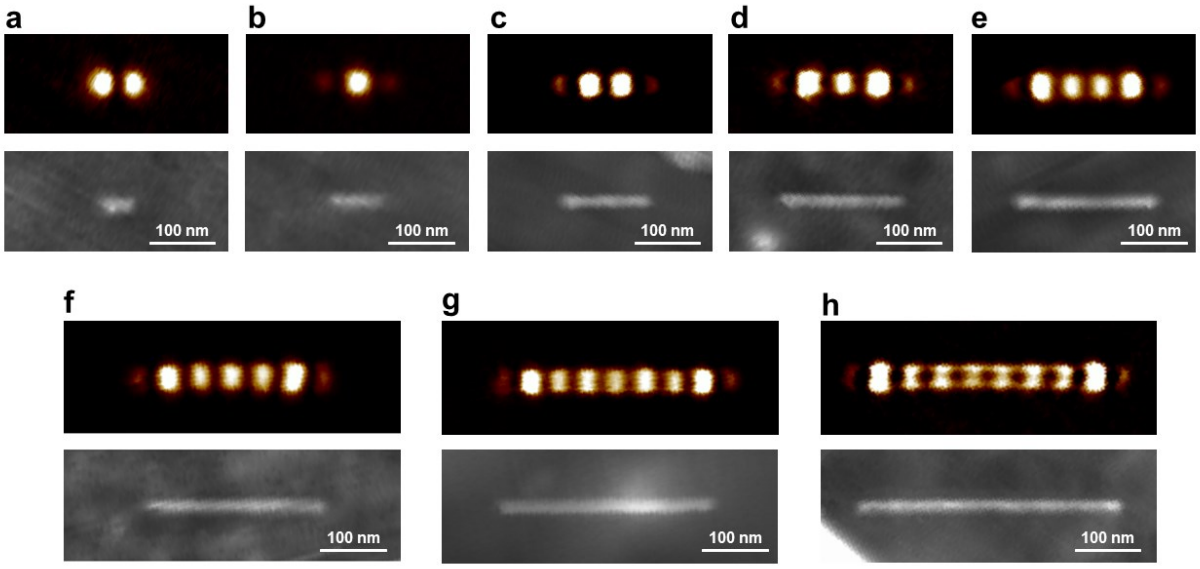

Figure 2. Infrared nano-imaging of SWNT nanocavities of different length. (a) to **(h)** Topography and corresponding near-field images for nanocavities with length ranging from 30 to 370 nm. In **(a)**, the shortest cavity ~ 30 nm cannot support even a single standing wave mode and the near-field response has on defined maximum at the cavity's center. With increasing cavity length from 55 to 370 nm as shown in **(b)** to **(h)**, we clearly observe an increasing number l of near-field signal maxima from 1 to 8 along the nanotube, corresponding to the antinodes of the (l+1) th resonance order standing plasmon wave. The excitation wavelength is 10.6 μm for the infrared nano-imaging.

We employ this electrode-free SPL to tailor SWNTs into ultraclean nanocavities with controllable length ranging from 30 to 370 nm. The two nanocavities closest in length differ by 20 nm. Figure 2a-h show the topography images of different nanocavities and their corresponding near-field responses at a set excitation wavelength of 10.6 μm. Evidently, the plasmon modes depend dramatically on the length of the cavities. The nanotube nanocavities act as Fabry-Perot resonators for surface plasmons bouncing back and forth between the two ends of the cavity. The longitudinal cavity modes of the surface plasmon can be described by $2k_pL + 2\emptyset_R = 2\pi l$, where $k_p = 2\pi/\lambda_p$ is the plasmon wavevector, L is the length of the cavity, $\emptyset_R$ is the effective reflection phase by the ends and l is the resonance order. The shortest cavity ~ 30 nm cannot support even a single standing wave mode (Figure 2a) and the near-field response has no defined maximum at the cavity's center. With increasing cavity length from 55 to 370 nm

(Figure 2b-h), we clearly observe an increasing number l of near-field signal maxima from 1 to 8 along the nanotube, corresponding to the antinodes of the $(l+1)$th resonance order standing plasmon wave. The separation between adjacent maxima corresponds to half of the plasmon wavelength and remains unchanged. By plotting the resonance order number against the cavity length, we can extract an effective reflection phase $\emptyset_R \sim 0.70\pi$ from the intercept as shown in Figure S2.

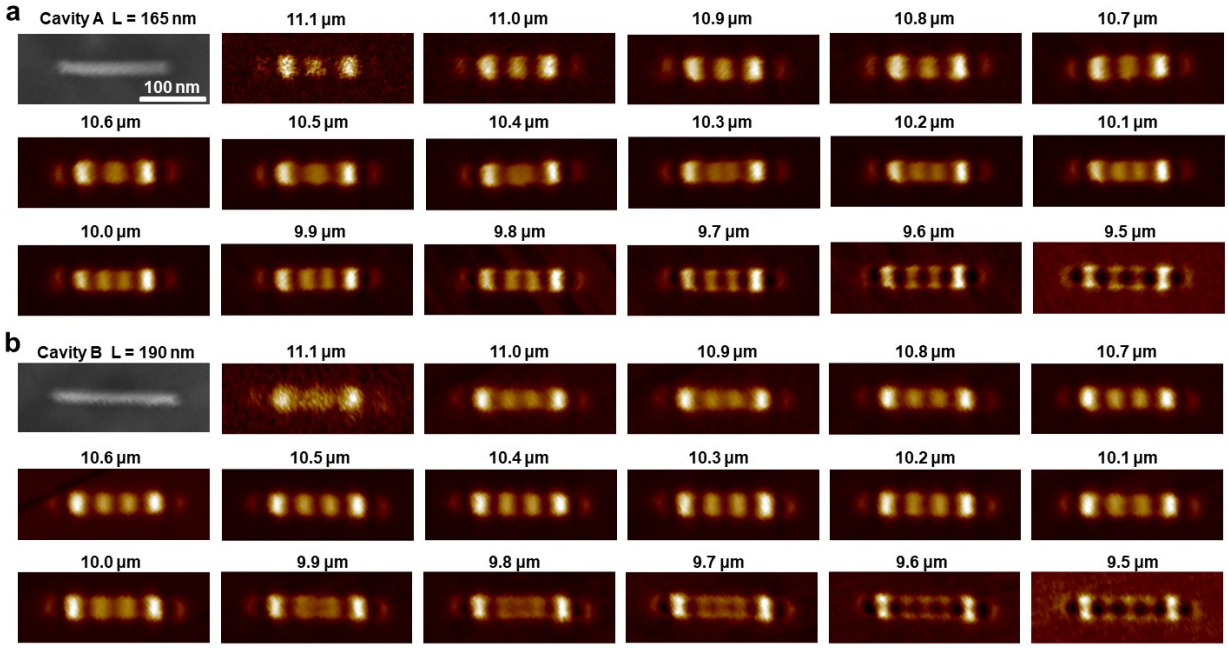

Figure 3. Spectral near-field responses of two SWNT nanocavities differing in length by about a quarter wavelength. (a) Topography and near-field images of nanotube cavity A with length ~ 165 nm at excitation wavelength from 11.1 to 9.5 μm. **(b)** Topography and near-field images of nanotube cavity B with length ~ 190 nm at excitation wavelength from 11.1 to 9.5 μm.

We further investigate the plasmon resonances in specific nanocavities by sweeping the wavelength of the excitation light λ_0, which sets the plasmon frequency ω and wavelength λ_p. We first perform infrared nano-imaging on a long nanotube without cavity effects for the whole wavelength range starting from 11.1 and decreasing to 9.5 μm. The infrared nano-imaging results and analysis for a representative long metallic nanotube are shown in Figures S3 and S4. As the excitation wavelength λ_0 is decreased from 11.1 to 9.5 μm, the plasmon wavelength λ_p shortens almost in a linear fashion from 98 to 76 nm. We then measure the wavelength-dependent plasmon modes in the nanocavities. Figures 3a and 3b show the near-field images of

two different nanotube cavities, denoted as cavity A and B, respectively. The near-field responses for each wavelength are normalized in amplitude by the responses of the long nanotube at the same wavelength to reveal the cavity effects. Figure 3a displays the topography image of cavity A with length ~ 165 nm and the evolution of its near-field plasmon modes with the excitation wavelength. At 11.1 and 9.5 μm, the near-field images feature three and four crisp equally-spaced maxima, respectively. Near 10.4 μm, however, a transition from three to four maxima occurs accompanied by a weakening and broadening of the center peak. In addition, Figure 3b shows cavity B with length ~ 190 nm along with its spectral near-field responses. While the length difference between cavity A and B is miniscule at about a quarter plasmon wavelength (~ 25 nm), this leads to strikingly different responses. Cavity B features 4 maxima in a well-defined sinusoidal wave pattern at around 10.4 μm while the transition to three and five maxima happens at 11.1 and 9.8 μm respectively. These behaviors can be qualitatively understood based on the plasmon cavity modes. The l = 4 and l = 5 plasmon cavity mode in A are resonantly excited at 11.1 and 9.5 μm laser wavelengths, respectively, while the l = 5 cavity mode in B is resonantly excited at 10.4 μm. The resonant modes exhibit a sinusoidal standing wave with well-defined nodes and antinodes. When the mode transition happens in cavity A at around 10.4 μm and in Cavity B at around 11.1 and 9.8 μm, the cavity resonance condition is not satisfied and a well-defined resonance mode cannot fit nicely within the cavity. The overall response profile deviates from the simple sinusoidal wave form with less pronounced nodes and antinodes.

To further examine the spectrally resolved plasmon interference patterns in detail, we plot in Figures 4b and 4d the line profiles of near-field responses along cavity A (Figure 3a) and B (Figure 3b). The evolution with excitation wavelength can be modeled by a Fabry-Perot resonator model of a plasmon nanowaveguide terminated by highly reflective ends. As schematically shown in Figure 4a, we assume that a plasmon wave of constant amplitude is locally excited at studied positions along the nanocavities. The wave will propagate in both directions and be reflected back and forth by the two ends and add together to produce a collective response. By repeating the summation process at different positions along the cavities, we can record the amplitude profiles as a function of position. The loss is characterized by the quality factor Q when the plasmon wave propagates in a damped oscillator form as $e^{-2\pi x/(Q\cdot\lambda_P)}\sin\left((4\pi x)/\lambda_p\right)$. The reflection at the ends features an amplitude approximated as

unity with a certain effective reflection phase $\emptyset_R$. The near-unity reflection amplitude originates from the large mode mismatch between the highly confined plasmon wave and the free space wave[22]. By adjusting the plasmon wavelength and quality factor obtained from infrared nano-imaging results for long metallic nanotubes (Figures S3 and S4), we acquire the simulated amplitude profiles for different excitation wavelengths from 11.1 to 9.5 μm.

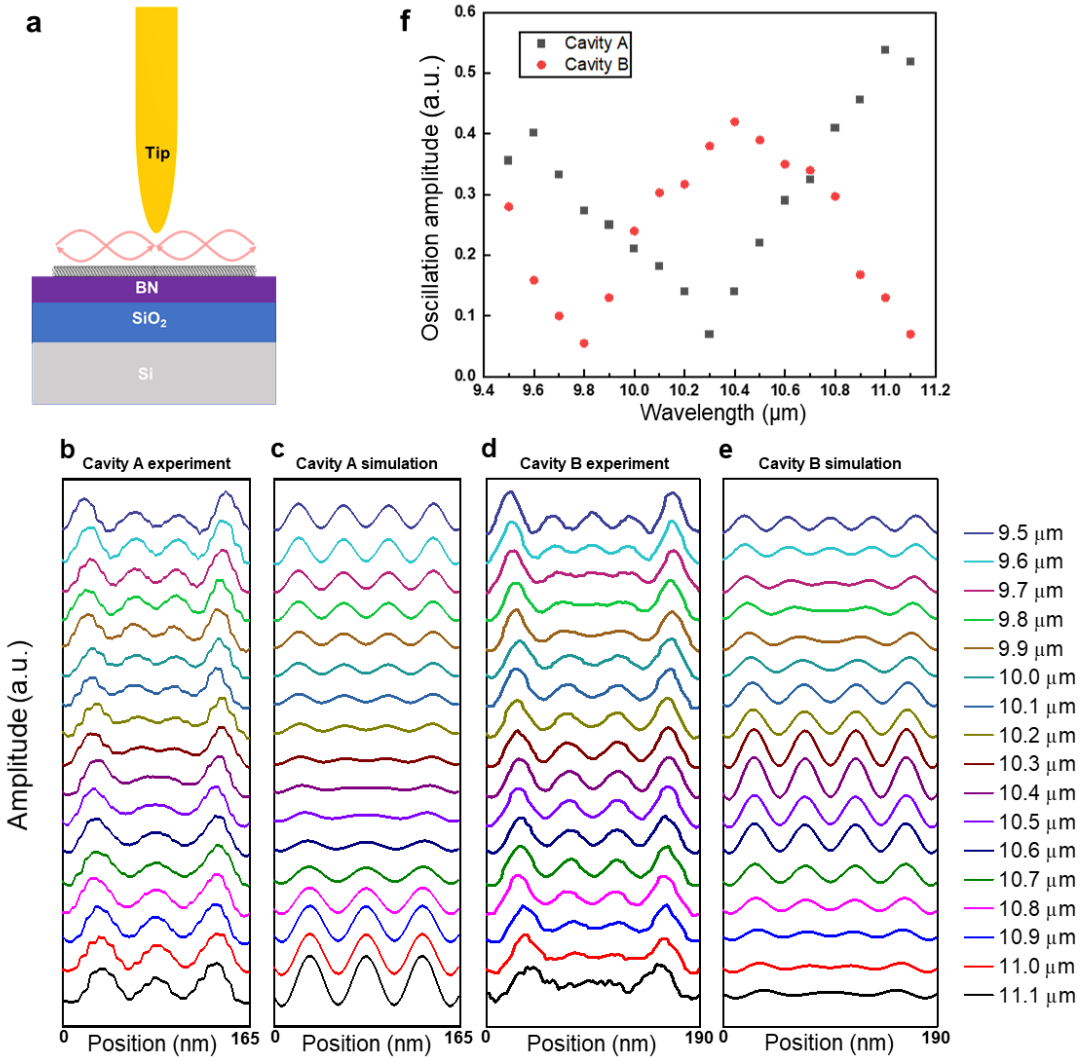

Figure 4. Comparison of experimental and simulated responses. (a) We assume that a plasmon wave of constant amplitude is locally excited at studied positions along the nanocavities. The wave will propagate in both directions and be reflected back and forth by the two ends and add together to produce a collective response. By repeating the summation process at different positions along the cavities, we can record the amplitude profiles as a function of position. **(b)** Experimental line profiles of near-field images of nanotube cavity A with length ~ 165 nm from

11.1 to 9.5 μm. **(c)** Simulated line profiles of nanotube cavity A by a lossy Fabry-Perot resonator model. **(d)** Experimental line profiles of near-field images of nanotube cavity B with length ~ 190 nm from 11.1 to 9.5 μm. **(e)** Simulated line profiles of nanotube cavity B by a lossy Fabry-Perot resonator model. The evolution of the experimental profiles with wavelength in the middle region of the cavity can be well captured by the model. **(f)** Experimental dependences of oscillation amplitude on excitation wavelength for cavity A and B.

The simulated profiles are shown in Figures 4c and 4e for comparison with experimental near-field responses shown in Figures 4b and 4d. The experimental antinodes near the ends of the cavities are noticeably stronger for all wavelengths. In addition, a relatively weak bright spot just outside the nanotube ends is also present in the experimental near-field images. Presumably, the phenomena arise from rather complicated coupling between the tip and the evanescent wave at the nanotube end. When the nanotube plasmon wave meets its ends, the guided plasmon wave experiences a diffraction due to discontinuity in conductivity. The diffraction leads to a nonpropagating near-field evanescent wave near the ends in addition to the reflected propagating plasmon wave. The presence of the evanescent wave results in a stronger field of the antinodes near nanotube ends and a relatively weak field just outside the ends. The modified field distribution is captured by infrared nano-imaging. Similar phenomena have been reported in edge reflections of graphene plasmons[22]. A detailed study of the phenomena in end reflections of nanotube plasmons is outside of the scope of this paper and will be reported elsewhere. Our model here accounts for the effects of the propagating wave and captures the evolution in the middle region. At 11.1 μm, cavity A is resonantly excited at order $l = 4$ and the plasmon mode shows a prominent sinusoidal wave form. The resonance condition increasingly deviates from $l = 4$ when the excitation wavelength is decreased from 11.1 to 10.4 μm, resulting in a systematic broadening and weakening of the center maxima. When the excitation wavelength is further decreased from the transition point (10.4 μm) to 9.5 μm, there is a gradual approach towards the resonance condition $l = 5$. Consequently, we see an increasing response amplitude in a better-defined sinusoidal wave form. Cavity B is longer than cavity A by about a quarter plasmon wavelength. At 10.4 μm excitation, we observe a prominent sinusoidal wave form corresponding to resonance order $l = 5$. Away from this resonance condition, there is a larger deviation from the sinusoidal wave with less pronounced nodes and antinodes. The experimental dependences of oscillation amplitude on excitation wavelength for cavity A and B are plotted in

Figure 4f, exhibiting inverse trends. Cavity B has a well-defined plasmon resonance peak for our wavelength range. Assuming a constant quality factor Q within the wavelength range, we estimate Q of cavity B to be $\frac{\lambda_r}{\Delta\lambda_r} \sim 11.6$, where $\lambda_r \sim 10.4\ \mu m$ is the resonance wavelength for cavity B and $\Delta\lambda_r \sim 0.9\ \mu m$ is the width of the resonance peak. This estimated Q is within the range of those extracted from the imaging measurements in Figures S3 and S4. The dramatic dependence of the plasmon resonances on cavity length highlights the high quality and tunability of these resonators. This can have intriguing implications for wavelength selective applications such as plasmon filtering and sensing. For example, by finely controlling the cavity length and the corresponding resonance frequency, we can match the cavity resonance mode to the vibrational fingerprints of certain molecules, achieving strong resonant coupling and therefore higher sensitivity.

We would like to remark that various metallic nanostructures, notably silver nanowires, have been proposed as plasmonic Fabry-Perot resonators in the visible and near-infrared range[23,24]. The plasmon spatial confinement characterized as λ_0/λ_p is typically around a few, which is much smaller than ~ 100 for SWNT cavities. The 1D plasmons in SWNTs with diameter ~ 1 nm feature even stronger transverse confinement ~ 1 nm, and the total mode volume is $V_p < 10^{-8}\ {\lambda_0}^3$. In addition, SWNT cavities have relatively lower dissipation during propagation and are also almost free from radiation damping upon reflection at cavity ends, which is evidenced by their near-unity reflection amplitude due to the large mode mismatch with free space wave[22]. SWNT cavity-based plasmonic resonators also compare favorably to those based on graphene ribbon nanostructures, offering a higher field confinement and lower loss. Particularly, SWNT cavities do not have edges, thus avoiding additional loss mechanisms whereas the structural imperfections and contaminations at the edges of graphene nanostructures after lithography or etching can severely degrade the quality factor[25-27]. The combination of high quality factor (Q > 10) and ultra-small mode volume $V_p < 10^{-8}\ {\lambda_0}^3$ has interesting implications for enhanced light-matter interaction, for instance, in terms of Purcell factor, which describes spontaneous emission modified by the coupling to an optical cavity. A quantum emitter near the SWNT nanocavity should experience a Purcell enhancement factor $F_p = \frac{3}{4\pi^2}({\lambda_0}^3)(\frac{Q}{V_p})$ exceeding 10^8. This is at least one order of magnitude larger than that reported so far with graphene nanoresonators or h-BN nanostructures[7,25,26] and approaches the ultimate plasmon

confinement limit[28,29]. In addition, the coupling efficiency of an emitter to the SWNT plasmons (i.e., the fraction of decay into plasmons) has also been suggested to reach values nearing 100% over a very broad range of emitter-SWNT distances and emitter/plasmon frequencies[16]. The strong and efficient coupling between emitters and SWNT plasmons can in turn greatly affect the plasmon resonances of SWNT cavities. Therefore, SWNT cavities can act as ultracompact and ultrasensitive nanosensors by monitoring the changes in their plasmon responses. For a broad spectrum from near-infrared to terahertz light, SWNT plasmonic nanocavities could serve in a role analogous to that of metallic nanostructures for visible frequencies.

Conclusion

In summary, advanced SPL is employed to tailor SWNTs into ultraclean nanocavities of controllable sizes. We then perform systematic spectrally resolved infrared nano-imaging of the plasmon resonances in these individual nanocavities. Assisted by theoretical modeling, the resonance behaviors can be well interpreted by a Fabry-Perot resonator model of a plasmon nanowaveguide terminated by highly reflective ends. We demonstrate that metallic SWNT nanocavities serve as one of the most compact nano-plasmonic elements with exceptional tunability and low loss. They can be further integrated, for instance, as nanoscale interconnects in nanophotonic circuits to facilitate plasmon coupling and detection. Plasmonic resonators based on metallic SWNTs nanocavities offer a viable route towards exceedingly strong and efficient light-matter interaction regime and show great promises in various appealing applications such as nanoscale lasers and amplifiers, quantum nano-optics, nonlinear nano-optics and ultra-sensitive plasmonic nanosensors potentially down to single molecules[15-21,30].

Methods

Carbon nanotube growth.

Ferritin solution (0.1 mmol/L) is drop-casted onto SiO_2 (285 nm)/Si substrates. The substrates are incubated at room temperature for 10 minutes. The substrates are rinsed with isopropyl alcohol (IPA) and are subsequently blow-dried. We anneal the substrates in air at 900 ℃ for 30 minutes to convert ferritin to Fe_2O_3 nanoparticles. Hexagonal boron nitride (h-BN) flakes are

mechanically exfoliated onto the Si substrates with Fe_2O_3 nanoparticles. We put the substrates into a one-inch quartz tube of an ambient-pressure CVD system. The system is firstly purged with hydrogen gas for 10 minutes to get rid of the air. After that, the temperature is raised to 900 °C in 15 minutes under 300 sccm of hydrogen flow. When the temperature reaches 900 °C, 110 sccm of argon is introduced through a bubbler with ethanol, working as the carbon precursor. 300 sccm of hydrogen flow is maintained to reduce iron compound nanoparticles to iron nanoparticles, which act as catalysts for SWNT growth. The temperature is kept at 900 °C for 15 minutes, followed by naturally cooling down to room temperature under a hydrogen flow of 300 sccm.

Infrared nano-imaging of carbon nanotube plasmons. The scattering-type IR-SNOM for this work is based on a tapping mode AFM (Bruker Innova). For infrared nano-imaging, a QCL (Daylight Solutions MIRcat) laser with tunable wavelength from 11.1 to 9.5 μm is focused onto the apex of a gold-coated AFM tip (Nanoandmore HQ:NSC15/Cr-Au-100) with a radius of tip apex ~ 20 nm. The excitation power is ~ 5 mW before the focusing lens (ZnSe aspherical lens with a numerical aperture of 0.42) and the spot size after focusing is ~ 20 μm. The tapping frequency and amplitude of the tip are Ω ~ 240 kHz and ~ 80 nm, respectively. The backscattered signal from the tip apex carries local optical information of the sample and is captured by a mercury cadmium telluride (MCT) detector (Kolmar Technologies KLD-0.1-J1/11/DC) in the far field. The detector signal is demodulated at a frequency 3Ω by a lock-in amplifier (Zurich Instruments HF2LI) to suppress the background scattering from the tip shaft and sample. By a raster scanning of the sample, near-field images are obtained simultaneously with the topography. We first perform infrared nano-imaging on a long nanotube without cavity effects for the whole wavelength range. The near-field responses of nanotube nanocavities for each wavelength are then normalized in amplitude by the responses of the long nanotube to reveal the cavity effects.

Electrode-free scanning probe lithography of carbon nanotubes. We first locate the long metallic carbon nanotubes by infrared nano-imaging. For electrode-free scanning probe lithography, AFM works in a contact-lift mode: during forward scanning, AFM works under the normal tapping mode, where the feedback is on for tracking the topography information; during backward scanning, the metallic AFM tip is lifted down by ~ 100 nm. We slide the tip across the nanotube at desired positions while applying a high-frequency AC voltage between the tip and the conductive Si layer of the substrate. This voltage generates a high-frequency AC current

which penetrates the SiO_2 layer via the capacitive coupling effect. During the nanoetching process, we apply an AC voltage with an amplitude of 15 V and a frequency of 40 kHz. Humidity should be maintained at higher than 45% for sufficient H_2O molecules to form a water bridge between the tip and the nanotube for the oxidation. The tip sliding velocity should be less than 5 μm/s to allow sufficient interaction time with the nanotube. The accuracy of the cavity length achievable by this top-down nanolithography method is limited by the radius of the tip apex, which is ~ 20 nm in our experiment.

ASSOCIATED CONTENT

Supporting Information.

(1) Helium ion microscopy (HIM) and nanopatterning of SWNTs, (2) Extraction of the effective reflection phase $\emptyset_R$, (3) Spectrally resolved infrared nano-imaging of a long metallic carbon nanotube, (4) Line profiles of near-field images in Figure S3 and plasmon analysis. This material is available free of charge via the Internet at http://pubs.acs.org.

Corresponding Author: fengwang76@berkeley.edu (F.W.)

Author contributions: F.W. and S.W. conceived the project and designed the experiments. F.W. and C.Z supervised the project. S.W. performed the nanolithography of the nanotubes, the infrared nano-imaging measurements and carried out the simulation. S.W. and F.W. analyzed the data. Fanqi W. grew the nanotubes under the supervision of C.Z. K.W. and T.T. provided the h-BN crystals. S.W. and F.W. wrote the manuscript with inputs from all authors.

Notes: The authors declare no competing financial interest.

Acknowledgements: We acknowledge helpful discussions with Dr. Jihun Kang. We thank Dr. Frances Allen for help with Helium Ion Microscopy. We thank Dr. Zhiwen Shi and Hongyuan Li for introduction of the nanolithography technique. We thank Dr. Alexander Zibrov and Jiu Chang for proofreading the manuscript. This work was mainly supported by the Director, Office of Science, Office of Basic Energy Sciences, Materials Sciences and Engineering Division of the U.S. Department of Energy under Contract No. DE-AC02-05-CH11231 (sp2-Bonded Materials Program KC2207). The AFM-based nanolithography of nanotubes and data analysis were supported by the NSF award 1808635. Fanqi W. and C.Z. acknowledge National Science Foundation for financial support under Grant No. 769K521. K.W. and T.T. acknowledge support

from the Elemental Strategy Initiative conducted by the MEXT, Japan and the CREST (JPMJCR15F3), JST.

References:

[1] A. F. Koenderink, A. Alù, and A. Polman, Science **348**, 516 (2015).
[2] J. A. Schuller, E. S. Barnard, W. Cai, Y. C. Jun, J. S. White, and M. L. Brongersma, Nature Materials **9**, 193 (2010).
[3] D. K. Gramotnev and S. I. Bozhevolnyi, Nature Photonics **4**, 83 (2010).
[4] E. Ozbay, Science **311**, 189 (2006).
[5] S. A. Maier, *Plasmonics: fundamentals and applications* (Springer Science & Business Media, 2007).
[6] J. B. Khurgin and G. Sun, in *Quantum Plasmonics*, edited by S. I. Bozhevolnyi, L. Martin-Moreno, and F. Garcia-Vidal (Springer International Publishing, Cham, 2017), pp. 303.
[7] M. Tamagnone, A. Ambrosio, K. Chaudhary, L. A. Jauregui, P. Kim, W. L. Wilson, and F. Capasso, Science Advances **4** (2018).
[8] F. J. Alfaro-Mozaz *et al.*, Nature Communications **8**, 15624 (2017).
[9] S. Das Sarma and E. H. Hwang, Physical Review B **54**, 1936 (1996).
[10] S. Wang, F. Wu, S. Zhao, K. Watanabe, T. Taniguchi, C. Zhou, and F. Wang, Nano Letters **19**, 2360 (2019).
[11] Z. Shi, X. Hong, H. A. Bechtel, B. Zeng, M. C. Martin, K. Watanabe, T. Taniguchi, Y.-R. Shen, and F. Wang, Nature Photonics **9**, 515 (2015).
[12] R. Garcia, A. W. Knoll, and E. Riedo, Nature Nanotechnology **9**, 577 (2014).
[13] H. Li, Z. Ying, B. Lyu, A. Deng, L. Wang, T. Taniguchi, K. Watanabe, and Z. Shi, Nano Letters (2018).
[14] J.-Y. Park, Y. Yaish, M. Brink, S. Rosenblatt, and P. L. McEuen, Applied Physics Letters **80**, 4446 (2002).
[15] J. N. Anker, W. P. Hall, O. Lyandres, N. C. Shah, J. Zhao, and R. P. Van Duyne, Nature Materials **7**, 442 (2008).
[16] L. Martín-Moreno, F. J. G. de Abajo, and F. J. García-Vidal, Physical Review Letters **115**, 173601 (2015).
[17] A. W. Barnard, M. Zhang, G. S. Wiederhecker, M. Lipson, and P. L. McEuen, Nature **566**, 89 (2019).
[18] A. S. Kadochkin, S. G. Moiseev, Y. S. Dadoenkova, V. V. Svetukhin, and I. O. Zolotovskii, Opt. Express **25**, 27165 (2017).
[19] N. P. de Leon, B. J. Shields, C. L. Yu, D. E. Englund, A. V. Akimov, M. D. Lukin, and H. Park, Physical Review Letters **108**, 226803 (2012).
[20] X. He, H. Htoon, S. K. Doorn, W. H. P. Pernice, F. Pyatkov, R. Krupke, A. Jeantet, Y. Chassagneux, and C. Voisin, Nature Materials (2018).
[21] T. Uda, A. Ishii, and Y. K. Kato, ACS Photonics **5**, 559 (2018).
[22] J.-H. Kang, S. Wang, Z. Shi, W. Zhao, E. Yablonovitch, and F. Wang, Nano Letters **17**, 1768 (2017).

[23] M. Allione, V. V. Temnov, Y. Fedutik, U. Woggon, and M. V. Artemyev, Nano Letters **8**, 31 (2008).
[24] H. Ditlbacher, A. Hohenau, D. Wagner, U. Kreibig, M. Rogers, F. Hofer, F. R. Aussenegg, and J. R. Krenn, Physical Review Letters **95**, 257403 (2005).
[25] V. W. Brar, M. S. Jang, M. Sherrott, J. J. Lopez, and H. A. Atwater, Nano Letters **13**, 2541 (2013).
[26] A. Y. Nikitin *et al.*, Nat Photon **10**, 239 (2016).
[27] I. Soto Lamata, P. Alonso-González, R. Hillenbrand, and A. Y. Nikitin, ACS Photonics **2**, 280 (2015).
[28] R. Chikkaraddy *et al.*, Nature **535**, 127 (2016).
[29] D. Alcaraz Iranzo *et al.*, Science **360**, 291 (2018).
[30] P.-H. Ho, D. B. Farmer, G. S. Tulevski, S.-J. Han, D. M. Bishop, L. M. Gignac, J. Bucchignano, P. Avouris, and A. L. Falk, Proceedings of the National Academy of Sciences **115**, 12662 (2018).

Graphic for the table of contents: